



RESEARCH ARTICLE

# A new theoretical approach for the performance simulation of multijunction solar cells

Gianluca Timò<sup>1,2</sup> | Alessio Martinelli<sup>1</sup> | Lucio Claudio Andreani<sup>2</sup>

<sup>1</sup>Materials and Generation Technologies Department, RSE, Piacenza, Italy

<sup>2</sup>Department of Physics, University of Pavia, Pavia, Italy

**Correspondence**

Gianluca Timò, Materials and Generation Technologies Department, RSE, Strada Torre della Razza, le Mose, Piacenza 29100, Italy.  
Email: gianluca.timo@rse-web.it

**Funding information**

Research Fund for the Italian Electrical System, Grant/Award Number: Contract Agreement between RSE (formerly known as

## Abstract

A new theoretical approach is proposed for the performance simulation of multijunction (MJ) solar cells, starting from the weakness and strength of the Hovel model and of the transfer matrix method for describing the propagation of electromagnetic waves inside the solar cell structure. It is based on the scattering matrix method (SMM) and on a simplified generation function that allow describing with good accuracy the propagation of electromagnetic waves in the solar cell device, preserving, at the same time, the possibility of getting simple analytical solutions of the continuity equations. The numerical stability of the new theoretical approach is first demonstrated on triple junction InGaP/InGaAs/Ge solar cells, in which the Ge substrate is considered as the last layer (layer N) and then as the N-1 layer. Further, the new theoretical approach is applied to simulate the performance of thin quadruple junction (QJ) InGaP/InGaAs/SiGeSn/Ge solar cells, in two- and three-terminal configurations. Efficiency values of up to 45.1% and 44.9%, respectively, have been simulated at 1000x concentration, by considering the MJ limited by the InGaAs subcell. Finally, it is estimated that the QJ InGaP/InGaAs/SiGeSn/Ge solar cell has the potential to reach efficiencies over 50% by assuming proper antireflective coatings.

## KEY WORDS

concentrating photovoltaics, multijunction, performance simulation

## 1 | INTRODUCTION

The simulation of the multijunction (MJ) solar cell performances requires several calculation steps. In Figure 1, for example, we show a possible scheme of the necessary steps. Among them, the choice of the *generation function*, which has to be inserted in the continuity equation to get the generation rates of holes/electrons, is of particular importance. According to the solar cell structures whose performances have to be simulated, different mathematical models have been implemented in order to calculate the propagation of radiation inside the solar cell. Finite element analysis has been applied to take into account 2D effects,<sup>1</sup> while rigorous coupled-wave analysis has

been considered for solar cells with nanophotonic designs.<sup>2</sup> For MJ solar cells, the most applied mathematical models are the Hovel<sup>3</sup> and the transfer matrix method (TMM).<sup>4–6</sup> In particular, the analytical Hovel model is widely and successfully considered for calculating the performance of optically thick solar cell structures, while TMM has become the most applied mathematical method to evaluate the performances of MJ cell structures<sup>7–10</sup> and of some organic thin films,<sup>11</sup> where the thickness of the layers is comparable with the wavelength of radiation and where, therefore, interference effects have to be considered. However, if the advantage of TMM over the Hovel model is the ability to calculate more accurately the electromagnetic radiation inside the solar cell structure, its disadvantage is the higher

This is an open access article under the terms of the Creative Commons Attribution License, which permits use, distribution and reproduction in any medium, provided the original work is properly cited.

© 2020 The Authors. Progress in Photovoltaics: Research and Applications published by John Wiley & Sons, Ltd.

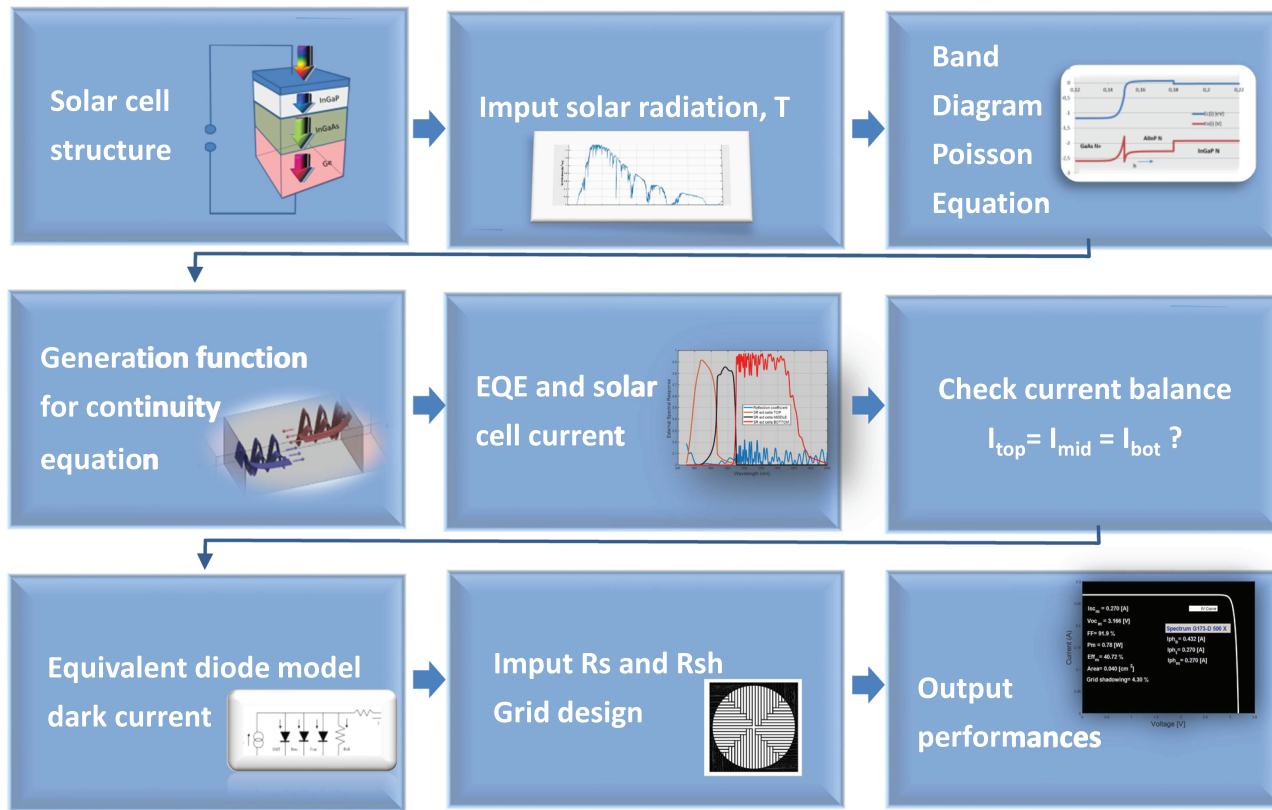


**FIGURE 1** Main steps for the calculation of the output performance of an MJ solar cell (as a particular case, a triple junction solar cell is considered) [Colour figure can be viewed at [wileyonlinelibrary.com](http://wileyonlinelibrary.com)]

complexity. In general, when the electromagnetic radiation in the solar cell layers is calculated by considering the interference of the forward and backward waves and inserted in the semiconductor continuity equation, it gives rise to solutions that are prohibitively complicated even for relatively few layers.<sup>12–14</sup> In particular, TMM presents an important weak point, as it suffers from numerical instability. For example, it has been reported that TMM fails in the determination of the reflection coefficient in the short wavelength range, when applied to the most recently designed MJ, in which the substrate is thinned and a mirror is deposited on the back side.<sup>15</sup>

It would be therefore very useful for the performance simulation of MJ solar cells to develop new mathematical approaches that preserve the simplicity of the Hovel model and, at the same time, offer the precision of the TMM for analysing the propagation of electromagnetic waves inside the solar cells structures, without suffering of numerical instability. With this contribution, a new mathematical approach that fulfils the above requirements is proposed. It is based on the utilization of a scattering matrix method (SMM) implemented from Yuffa and Scales<sup>16</sup> and on a simplified generation function that uses the radiation calculated by SMM and allows solving the continuity equation with good precision getting simple analytical solutions. This contribution is organized in the following parts: (a) The general assumptions at the basis of the mathematical models for the performance simulation of MJ solar cells are first introduced; (b) the salient features of the Hovel and TMM are then discussed; (c) the SMM and the simplified generation function are implemented; (d) the continuity

equations are solved analytically, and the robustness of the new mathematical approach is demonstrated on triple junction InGaP/InGaAs/Ge solar cells; and (e) the approach is then applied to simulate the performance of a thin quadruple junction (QJ) InGaP/InGaAs/SiGeSn/Ge solar cell, in two-terminal (2T) and three-terminal (3T) configurations.

## 2 | GENERAL ASSUMPTIONS

The mathematical models presented hereafter have all in common the following assumptions:

1. One dimension (edge effects are neglected).
2. Boltzmann approximation for the calculation of the carriers distribution. Nondegenerate semiconductors.
3. Low injection conditions.
4. All parameters, mobility, diffusion coefficient, and lifetime are assumed constant within each semiconductor material. Since the concentrations of dopant atoms in the base and emitter are assumed uniform (quasi-neutral region), the electric field value is zero outside the depletion region.
5. The mobility of minority carriers is assumed to depend on the doping of the side where majority carries are located. It should be pointed out that repulsive potentials scatter less than attractive potentials of the same strength<sup>17</sup>; therefore, the minority carrier

mobility is higher than the majority carrier mobility. If the majority carrier mobility values obtained by Hall measurements are assumed for minority carriers, the related minority diffusion length values will be lower than the actual ones.

6. The solar cell window absorbs the solar light; however, the carriers here produced by absorption are neglected for the computation of the photovoltaic current. This assumption can lead to underestimating the photovoltaic current, as reported in Létay et al.<sup>18</sup> The same assumption is applied for the back surface field (BSF) layers. The reason behind these assumptions is that such layers are very thin compared with base and emitter layers of the solar cell.
7. The tunnel current peak value of each tunnel diode (TD) is supposed to be higher than the solar cell short-circuit current value. Therefore, TD layers are considered only with respect to the light absorption. The series resistance of the TD is included in the total series resistance of the MJ device.
8. For each absorbed photon, an electron-hole pair is produced, that is, the photon absorption rate [ $n \cdot ph \text{ s}^{-1} \text{ m}^{-3} \text{ nm}^{-1}$ ] is equal to the carriers generation rate [ $n \cdot e^-/h^+ \text{ s}^{-1} \text{ m}^{-3} \text{ nm}^{-1}$ ].
9. Each subsolar cell of the MJ structure is divided into three parts: the two quasi-neutral regions of the emitter and the base and the space charge region. The continuity equations are solved in the quasi-neutral region to get the emitter and the base current densities. In the depletion region, owing the strong electric field, it is assumed that all the generated carries are swept in opposite directions and collected.
10. The generation terms owing to self-excitation<sup>19</sup> and photon coupling effects<sup>20</sup> are in first approximation neglected.

### 3 | HOVEL MODEL

The great advantage of the Hovel mathematical model is the simplicity of its generation function. In this model, multiple light reflections inside the photovoltaic active layers are neglected; therefore, the generation term,  $G$ , is calculated only considering a positive light flux,  $F(\lambda, x)$ , absorbed inside the cell's structure according to the Beer-Lambert law. The reflection coefficient,  $R(\lambda)$ , which takes into account the solar light reflected at the solar cells surface, is calculated only by considering the interference effects produced inside the coating and the solar cell window layer. By considering assumption 8 of Section 2, it holds the following:

$$F(\lambda, x) = [1 - R(\lambda)]F(\lambda, 0)e^{-\alpha(x)x}, \quad (3.1)$$

$$G(\lambda, x) = -\frac{dF(x, \lambda)}{dx} = \alpha(\lambda)F(\lambda)[1 - R(\lambda)]e^{-\alpha(x)x}, \quad (3.2)$$

where  $\lambda$  and  $x$  are the wavelength and the path travelled by light, respectively. The continuity equations, solved by considering the generation term given by Equation (3.2), give rise to simple and useful analytical solutions for the cell current, not here reported as they are

well documented in many solar cell text books (see, for example, Harold<sup>3</sup> and Nelson<sup>21</sup>).

### 4 | THE TMM

The TMM is a powerful mathematical method that takes into account the complex nature of the wave vector and allows considering the multiple reflections and interference phenomena of the forward and backward travelling waves. The calculated electromagnetic radiation by TMM can then be inserted in the semiconductor continuity equations to determine the photocarrier generation, replacing the flux term used by Hovel. A schematic representation of the MJ solar cell structure, generally composed of  $N$  layers, is reported in Figure 2, along with the possible coordinate systems.

The following general assumptions are usually considered:

1. the solar radiation propagates like a plane wave coming from the #0 layer (air);
2. the solar intensity is not polarized, and it can be thought as equally distributed in the TM and TE polarization modes;
3. the last layer (#N layer) is considered optically thick, and the reflected radiation at its back surface can be neglected;
4. each layer is homogeneous and isotropic;
5. source-free layers and interfaces (current density,  $J$ , and charge density,  $q$ , are set to zero).

The electromagnetic radiation inside the MJ structure is calculated by considering the source-free macroscopic Maxwell equations, with proper boundary conditions that ensure the continuity of the electric and magnetic fields at the interfaces. A system of  $2N$  equations is generated for each polarization mode, and it contains  $2N$  unknowns, ie, the complex amplitudes of the forward and backward waves at the beginning (or at the end) of each layer. In particular, it results that the complex amplitudes of the forward and backward waves at the beginning (or at the end) of a generic layer  $j$  ( $\mathbf{N}_j^+, \mathbf{N}_j^-$ ) are connected to the complex amplitudes of the forward and backward waves at the beginning (or at the end) of the adjacent layer  $j + 1$  ( $\mathbf{N}_{j+1}^+, \mathbf{N}_{j+1}^-$ ) through the characteristic layer matrix,  $T_j$  (or  $M_{j+1}$ ) as reported in Table 1.

The solution of the linear equations system given by Equation (13.1) or Equation (13.3) is easily obtained by considering a mathematical procedure that uses the matrix  $M$  (see Appendix A), given by the product of the characteristic layers matrix:

$$M = M_1 M_2 \dots M_N \rightarrow M = \begin{bmatrix} M_{11} & M_{12} \\ M_{21} & M_{22} \end{bmatrix}. \quad (4.1)$$

The reason of the numerical instability of TMM is due to the structure of the matrix  $M$ . As indicated by Equation (13.4), the matrix  $M_{j+1}$  and every characteristic layer matrix  $M_j$  of a generic layer,  $j$ , contain the terms  $\Psi_j^- = e^{-ik_j x d_j}$ . Therefore, the left half of the transfer matrix  $M$  given by Equation (4.1) grows exponentially as the

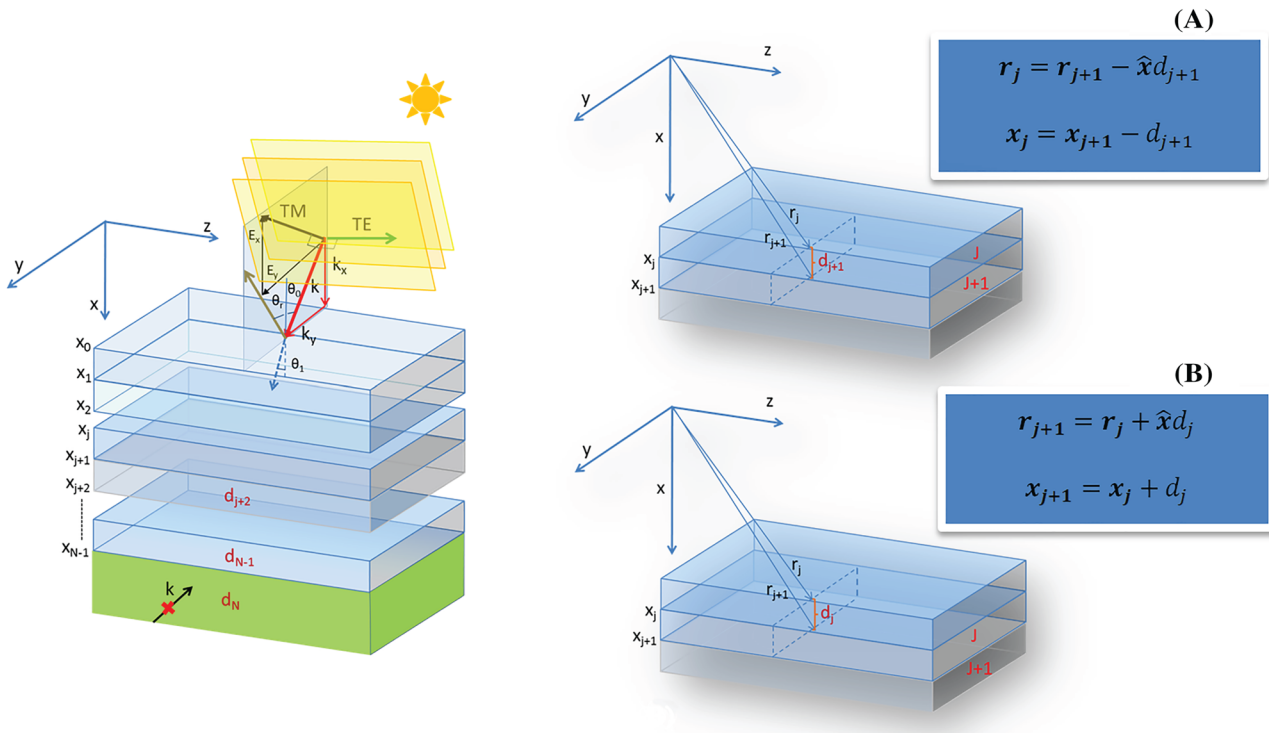


**FIGURE 2** Geometrical representation of the MJ solar cell layers and the coordinate systems. The two polarization modes (TM and TE) of the radiation are indicated. On the right, the two possible ways to identify the layer position are shown: A,  $r_j$  is the position vector that identifies the position at the end of the layer  $j$ ; B,  $r_j$  is the position vector that identifies the position at the beginning of the layer  $j$ ;  $d_j$  is the thickness of the layer  $j$  [Colour figure can be viewed at [wileyonlinelibrary.com](http://wileyonlinelibrary.com)]

**TABLE 1** The complex amplitudes of the forward and backward waves at the beginning and at the end of adjacent layers and the characteristic layer matrix

**Electromagnetic field at the beginning of layers  $j+1, j$**

$$\begin{bmatrix} \mathbf{N}_{j+1}^+ \\ \mathbf{N}_{j+1}^- \end{bmatrix} = T_j \begin{bmatrix} \mathbf{N}_j^+ \\ \mathbf{N}_j^- \end{bmatrix} \quad (13.1)$$

$$T_j = \frac{1}{2w_{j+1}} \begin{bmatrix} \Psi_j^+ (w_{j+1} + w_j) & \Psi_j^- (w_{j+1} - w_j) \\ \Psi_j^+ (w_{j+1} - w_j) & \Psi_j^- (w_{j+1} + w_j) \end{bmatrix} \quad (13.2)$$

**Electromagnetic field at the end of layers  $j, j+1$**

$$\begin{bmatrix} \mathbf{N}_j^+ \\ \mathbf{N}_j^- \end{bmatrix} = M_{j+1} \begin{bmatrix} \mathbf{N}_{j+1}^+ \\ \mathbf{N}_{j+1}^- \end{bmatrix} \quad (13.3)$$

$$M_{j+1} = \frac{1}{2w_j} \begin{bmatrix} \Psi_{j+1}^- (w_j + w_{j+1}) & \Psi_{j+1}^+ (w_j - w_{j+1}) \\ \Psi_{j+1}^- (w_j - w_{j+1}) & \Psi_{j+1}^+ (w_j + w_{j+1}) \end{bmatrix} \quad (13.4)$$

TM

$$\Psi_j^\pm = e^{\pm ik_{j,x}d_j}, \quad k_{j,x} = \frac{2\pi}{\lambda_0} n_j \cos \theta_j \quad (13.5)$$

$$w_j = \frac{\epsilon_j}{k_{j,x}} \quad (13.6)$$

$$\mathbf{N}_j^\pm = \pm k_{j,x} \mathbf{E}_j^\pm e^{\pm ik_{j,x}x_j} \quad (13.8)$$

TE

$$w_j = \frac{k_{j,x}}{\mu_j} \quad (13.7)$$

$$\mathbf{N}_j^\pm = \mathbf{E}_j^\pm e^{\pm ik_{j,x}x_j} \quad (13.9)$$

Notes. For the layer  $j$ ,  $k_{j,x} = x$  component of the complex wave number;  $n_j$  complex refractive index;  $\epsilon_j$  = complex permittivity;  $\mu_j$  = complex permeability.

number of layers (or thickness of a single layer) increases. We can thus expect to find a numerical instability when the MJ structure reaches a certain total thickness. As already mentioned, this was observed on solar cell structures designed to improve the voltage. In

order to overcome this problem, the TMM has to be replaced with another mathematical method that does not become unstable as the number of MJ layers increases. The SMM fulfils the requirement of the numerical stability.

## 5 | THE SMM

The simple S-matrix formulation suggested in Yuffa and Scales<sup>16</sup> is a suitable alternative method that can be applied to study the electromagnetic fluxes in MJ solar cells. The calculation of the S-matrix elements is hereafter reported by considering the complex amplitudes of the forward and backward waves at the end of adjacent layers. A similar procedure can be followed considering the complex amplitudes of forward and backward waves at the beginning of adjacent layers (see Appendix B).

In the S-matrix method, the outgoing waves are connected to the incoming waves. In particular, the layer scattering matrix  $S_j$  is built up in such a way to connect the outgoing and incoming waves of the generic  $j$  layer with the outgoing and incoming waves of the last layer,  $N$ :

$$\begin{pmatrix} \Psi_j^- \\ \Psi_N^+ \end{pmatrix} = S_j \begin{pmatrix} \Psi_j^+ \\ 0 \end{pmatrix} = \begin{bmatrix} S_j(1,1) & S_j(1,2) \\ S_j(2,1) & S_j(2,2) \end{bmatrix} \begin{pmatrix} \Psi_j^+ \\ 0 \end{pmatrix}. \quad (5.1)$$

The  $S_j$ -matrix elements are calculated by forcing the compatibility of the system of Equation (13.3) with the system of Equation (5.1), therefore considering the following:

$$\Psi_j^\pm = \psi_j^\pm. \quad (5.2)$$

Developing Equation (13.3), we have the following:

$$\begin{cases} \Psi_j^+ = M_{j+1}(1,1)\Psi_{j+1}^+ + M_{j+1}(1,2)\Psi_{j+1}^- \\ \Psi_j^- = M_{j+1}(2,1)\Psi_{j+1}^+ + M_{j+1}(2,2)\Psi_{j+1}^- \end{cases} \quad (A) \quad (B) \quad (5.3)$$

while Equation (5.1) can be written as follows:

$$\begin{cases} \Psi_j^- = S_j(1,1)\Psi_j^+ \\ \Psi_N^+ = S_j(2,1)\Psi_j^+ \end{cases} \quad (C) \quad (D) \quad (5.4)$$

For  $j = N$ , Equation (5.4) becomes

$$\begin{cases} \Psi_N^- = S_N(1,1)\Psi_N^+ \\ \Psi_N^+ = S_N(2,1)\Psi_N^+ \end{cases} \quad (5.5)$$

Since  $\Psi_N^- = 0 \rightarrow S_N(1,1) = 0$  and  $S_N(2,1) = 1$ .

By considering the above relationships, the compatibility of the system of Equation (5.3) with the system of Equation (5.4) allows calculating the scattering matrix elements:

$$S_j(1,1) = \frac{(w_j - w_{j+1}) + (\psi_{j+1}^+)^2(w_j + w_{j+1})S_{j+1}(1,1)}{(w_j + w_{j+1}) + (\psi_{j+1}^+)^2(w_j - \beta w_{j+1})S_{j+1}(1,1)}, \quad (5.6)$$

$$S_j(2,1) = \frac{2w_j\psi_{j+1}^+ S_{j+1}(2,1)}{(w_j + w_{j+1}) + (w_j - \beta w_{j+1})S_{j+1}(1,1)(\psi_{j+1}^+)^2}. \quad (5.7)$$

The outgoing and incoming waves in each layer, for TM and TE polarization, can be easily calculated, considering that from Equation (5.4)D, for  $j = 0$ , it holds the following:

$$\Psi_0^+ = \frac{\Psi_N^+}{S_0(2,1)}. \quad (5.8)$$

The electric field  $\Psi_0^+$  propagating in the layer "0" (air) in the positive direction (towards the solar cell surface) can be calculated from the flux of the Poynting vector of the solar radiation. Therefore, from Equation (5.8), we can get  $\Psi_N^+$  and, therefore, from Equation (5.4) and Equation (5.7) all  $\Psi_j^+$  and  $\Psi_j^-$ .

## 6 | A SIMPLIFIED GENERATION FUNCTION

The energy flux through each interface is calculated by means of the flux of the Poynting vector, for TM and TE modes. In the layer  $j$ , the Poynting vector at position  $r_j$  is given by the following:

$$\langle \tilde{s}_j(r_j) \rangle = \frac{1}{2} \operatorname{Re} [E_j(r_j, t) \times H_j(r_j, t)^*]. \quad (6.1)$$

The symbol  $\langle \rangle$  means that we are considering the average of the Poynting vector, since the integration time of the measurement of the electromagnetic radiation is much longer than the period of the wave. By considering that the Poynting vector does not change on the plane  $yz$  (owing to assumption 4 of Section 4), the energy crossing a surface in unit time and unit surface (the flux of the Poynting vector):

$$\varphi(S) = \int \int S \cdot n da, \quad (6.2)$$

where  $n$  is the normal is simply given by the following:

$$\langle \tilde{s}_j(r_j) \rangle \cdot \hat{x}. \quad (6.3)$$

It can be shown that

$$\langle \tilde{s}_j(r_j) \rangle \cdot \hat{x} = \langle \tilde{s}_j(x_j) \rangle^+ + \langle \tilde{s}_j(x_j) \rangle^- + \langle \tilde{s}_j(x_j) \rangle^\pm, \quad (6.4)$$

where  $\langle \tilde{s}_j(x_j) \rangle^+$  represents the energy current density owing to the electric field propagating in the  $x$  positive direction,  $\langle \tilde{s}_j(x_j) \rangle^-$  represents the energy current density owing to the electric field propagating in the  $x$  negative direction, while  $\langle \tilde{s}_j(x_j) \rangle^\pm$  represents the energy current density oscillatory terms due to interference between the counter-propagating waves, whose expressions for TM and TE mode are reported in Table 2.

**TABLE 2** Energy current density owing to the electric field propagating in the positive, negative direction and due to the counter propagating waves interference

TM	TE
$\langle \tilde{S}_j(x_j) \rangle^+_{TM} = \frac{1}{2} \operatorname{Re}[e_j^* k_{j,x}] \omega \frac{ N_j^+ ^2}{ k_{j,x} ^2}$ (13.10)	$\langle \tilde{S}_j(x_j) \rangle^+_{TE} = \frac{1}{2\omega} \operatorname{Re}\left[\frac{k_{j,x}}{\mu_j}\right]  N_j^+ ^2$ (13.11)
$\langle \tilde{S}_j(x_j) \rangle^-_{TM} = -\frac{1}{2} \operatorname{Re}[e_j^* k_{j,x}] \omega \frac{ N_j^- ^2}{ k_{j,x} ^2}$ (13.12)	$\langle \tilde{S}_j(x_j) \rangle^-_{TE} = -\frac{1}{2\omega} \operatorname{Re}\left[\frac{k_{j,x}^*}{\mu_j^*}\right]  N_j^- ^2$ (13.13)
$\langle \tilde{S}_j(x_j) \rangle^\pm_{TM} = \frac{1}{2} \frac{\omega}{ k_{j,x} ^2} \operatorname{Re}\left\{ e_j^* k_{j,x} [N_j^- N_j^{+*} - N_j^+ N_j^{-*}] \right\}$ (13.14)	$\langle \tilde{S}_j(x_j) \rangle^\pm_{TE} = \frac{1}{2\omega} \operatorname{Re}\left\{ \frac{k_{j,x}}{\mu_j} [N_j^- N_j^{+*} - N_j^+ N_j^{-*}] \right\}$ (13.15)

Notes. The symbol \* indicates the complex conjugate;  $\omega$  = angular frequency.

In order to get the generation function to be used to solve the continuity equation, we have to show how the Poynting vector is changing within each layer. For the moment, let us assume that we can neglect the energy current density oscillatory term due to the interference between the counter propagating waves (Equations 13.14 and 13.15); this assumption will be later assessed.

Considering the complex amplitudes of the forward and backward waves at the end of the layer, that is, in  $x_j$ , and changing the position  $x$  towards the beginning of a layer (negative direction), it straightforward to show that

$$\langle \tilde{S}_j(x_j-x) \rangle^+_{TM, TE} = \langle \tilde{S}_j(x_j) \rangle^+_{TM, TE} e^{2Im(k_{j,x})x}, \quad (6.5)$$

$$\langle \tilde{S}_j(x_j-x) \rangle^-_{TM, TE} = \langle \tilde{S}_j(x_j) \rangle^-_{TM, TE} e^{-2Im(k_{j,x})x}. \quad (6.6)$$

Equations (6.5) and (6.6) tell us that the energy flux propagates inside each layer by following a “generalized” Beer-Lambert law. The factor  $2Im(k_{j,x})$ , where  $Im$  stands for the imaginary part, is exactly equal to the absorption coefficient in case of perpendicular incidence. Similar expressions, with the exponential terms inverted in sign, characterize the TM and TE energy current density variation considering the complex amplitudes of the forward and backward waves at the beginning of the layer and changing  $x$  towards the end of a layer (positive direction).

By assuming that each layer,  $j$ , starts at coordinate  $x_0$  and ends at coordinate  $x_N$ , we indicate with  $F_j^+(x_0, \lambda)$ , the photon flux at the beginning of the layer, in  $x_0$ , propagating in the positive  $x$  direction, and with  $F_j^-(x_N, \lambda)$ , the photon flux at the end of the layer, in  $x_N$ , propagating in the negative  $x$  direction. It holds the following:

$$F_j^+(x_0, \lambda) = \frac{\left\{ \langle \tilde{S}_j(x_0) \rangle^+_{TE} + \langle \tilde{S}_j(x_0) \rangle^+_{TM} \right\} \lambda}{hc}. \quad (6.7)$$

$$F_j^-(x_N, \lambda) = \frac{\left\{ \langle \tilde{S}_j(x_N) \rangle^-_{TE} + \langle \tilde{S}_j(x_N) \rangle^-_{TM} \right\} \lambda}{hc}. \quad (6.8)$$

The generation rate for the positive and negative fluxes is then given by the following:

$$G^\pm(\lambda, x) = \mp \frac{dF(x, \lambda)}{dx}; \quad (6.9)$$

therefore, with  $x_0 < x < x_N$ , it can be written as follows:

$$G_j(x, \lambda) = 2Im[k_{j,x}(\lambda)] \left[ F_j^+(x_0, \lambda) e^{2Im[k_{j,x}(\lambda)](x_0-x)} + F_j^-(x_N, \lambda) e^{2Im[k_{j,x}(\lambda)](x-x_N)} \right]. \quad (6.10)$$

The generation function of Equation (6.10) is a generalization of the Hovel generation function given by Equation (3.2), in which the absorption coefficient has been replaced by the term  $2Im(k_{j,x})$  (which then allows considering the different wave propagation angle); we have added the contribution of the negative flux generated by the reflection at the different interfaces and the positive and negative fluxes take into account interference effects. A similar expression of the generation rate has been considered in Kowalczewski.<sup>22</sup>

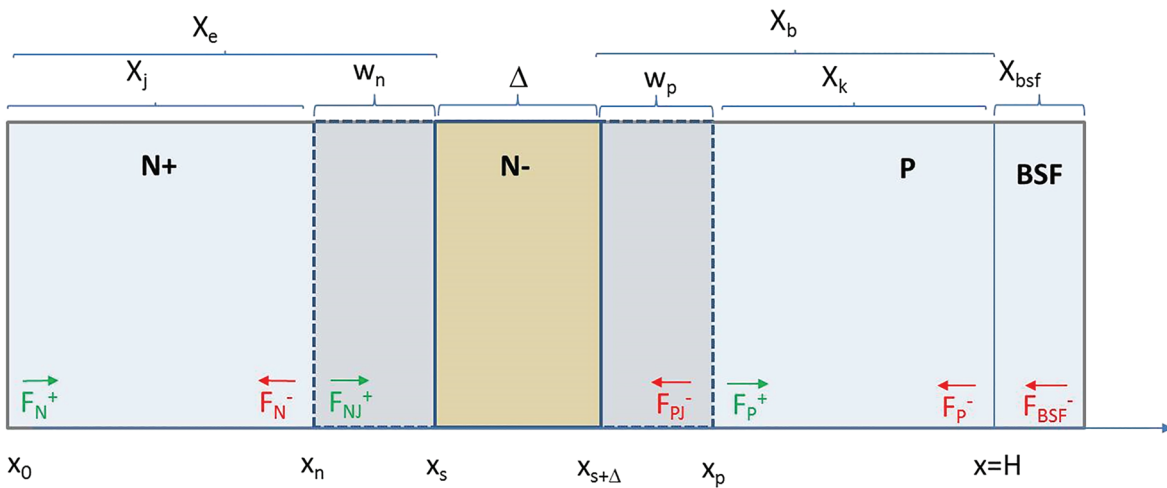
## 7 | ANALYTIC SOLUTION OF THE CONTINUITY EQUATION

Figure 3 shows a generic single junction cell structure, which can be thought as a subcell of an MJ structure. The solar cell includes an intrinsic material (or a slightly doped material, N–), called spacer, inserted between the emitter (N+) and the base (P) and a “BSF” layer. For the cell structure reported in Figure 3, the flows  $F_N^+$  and  $F_{BSF}^-$  are directly calculated by SMM; the other ones are determined by using the generalized Lambert-Beer law. The analytic expressions of the current density in the emitter, in the depletion region, and in the base are calculated in the following.

### 7.1 | Determination of $J_p$

By considering Equation (6.10), the generation function for the emitter becomes

$$G_p = 2Im(k) \left[ F_N^+ e^{-2Im(k)x} + F_N^- e^{2Im(k)(x-x_N)} \right], \quad (7.1)$$



**FIGURE 3** Schematic of a generic SJ cell structure (without the window layer) considering the same materials for all the layers. The photon flux to be considered in the continuity equation is indicated [Colour figure can be viewed at [wileyonlinelibrary.com](http://wileyonlinelibrary.com)]

$$\frac{dy}{dx} = \eta_p y \quad \text{at } X=0 \quad (7.7)$$

where  $x_0$  has been assumed equal to zero without losing generality.

By considering assumption 4 of Section 2, the continuity equation can be written as follows:

$$-\frac{1}{q} \frac{d}{dx} \left( q D_p \frac{d(p_n - p_{n0})}{dx} \right) - G_p + \frac{p_n - p_{n0}}{\tau_p} = 0, \quad (7.2)$$

where  $D_p$  is the hole diffusion coefficient and  $\tau_p$  is the hole lifetime. In Equation (7.2), the equilibrium hole concentration in the emitter,  $p_{n0}$ , has also been considered as position independent.

By setting

$$y = (p_n - p_{n0}) L_p^3; L_p = \sqrt{D_p \tau_p}; X = \frac{x}{L_p} \quad (7.3)$$

and

$$f_N^+ = \tau_p L_p^3 2 \operatorname{Im}(k) F_N^+; f_N^- = \tau_p L_p^3 2 \operatorname{Im}(k) F_N^-; \beta_p = 2 L_p \operatorname{Im}(k), \quad (7.4)$$

Equation (7.2) becomes

$$\frac{d^2y}{dx^2} + f_N^+ e^{-\beta_p X} + f_N^- e^{\beta_p(X-X_N)} - y = 0. \quad (7.5)$$

The generic solution of Equation (7.5) is as follows:

$$y = A_p \cosh X + B_p \sinh X + \frac{f_N^+ e^{-\beta_p X} + f_N^- e^{\beta_p(X-X_N)}}{1 - \beta_p^2}. \quad (7.6)$$

The constants  $A_p$ ,  $B_p$  can be determined by applying the usual two boundary conditions:

with  $\eta_p = \frac{S_p L_p}{D_p}$ , where  $S_p$  is the holes recombination velocity, and

$$y = 0 \quad \text{at } X = X_N = X_e - \frac{w_n}{L_p}. \quad (7.8)$$

From Equation (7.7), it follows:

$$B_p = \eta_p A_p + \frac{f_N^+ (\eta_p + \beta_p) + f_N^- (\eta_p - \beta_p) e^{-\beta_p X_N}}{1 - \beta_p^2}. \quad (7.9)$$

From Equation (7.8) and considering Equation (7.9), it holds the following:

$$A_p = \frac{f_N^+ [(\eta_p + \beta_p) \sinh X_N + e^{-\beta_p X_N}] + f_N^- [(\eta_p - \beta_p) e^{-\beta_p X_N} \sinh X_N + 1]}{(\beta_p^2 - 1) (\cosh X_N + \eta_p \sinh X_N)}. \quad (7.10)$$

In the quasi-neutral emitter region, the current density is purely diffusive and can be calculated in  $X_N$ , by the following:

$$J_p(X_N) = -q D_p \frac{1}{L_p^4} \frac{dy}{dx} \Big|_{X_N}, \quad (7.11)$$

$$J_p(X_N) = -q D_p \frac{1}{L_p^4} \left[ A_p \sinh X_N + B_p \cosh X_N + \beta \frac{f_N^- - f_N^+ e^{-\beta_p X_N}}{1 - \beta_p^2} \right], \quad (7.12)$$

where  $A_p$  and  $B_p$  are given respectively by Equations (7.10) and (7.9).

## 7.2 | Determination of $J_n$

By considering Equation (6.10), the generation function for the base is as follows:

$$G_n = 2\text{Im}[k(\lambda)] \left[ F_p^+ e^{2\text{Im}(k)(x_p-x)} + F_p^- e^{2\text{Im}(k)(x-h)} \right]. \quad (7.13)$$

By considering assumption 4 of Section 2, the continuity equation can be written as follows:

$$\frac{1}{q} \frac{d}{dx} \left( qD_n \frac{d(n_p - n_{p0})}{dx} \right) + G_n - \frac{n_p - n_{p0}}{\tau_n} = 0, \quad (7.14)$$

where  $D_n$  is the electrons diffusion coefficient and  $\tau_n$  is the electrons lifetime. In Equation (7.14), the equilibrium electron concentration in the base,  $n_{p0}$ , has also been considered position independent.

By setting

$$y = (n_p - n_{p0})L_n^3; L_n = \sqrt{D_n \tau_n}; X = \frac{x - x_p}{L_n} \quad (7.15)$$

and

$$f_p^+ = \tau_n L_n^3 2\text{Im}(k) F_p^+; f_p^- = \tau_n L_n^3 2\text{Im}(k) F_p^-; \beta_n = 2L_n \text{Im}(k); X_p = \frac{x_p}{L_n}; h = \frac{H}{L_n}, \quad (7.16)$$

Equation (7.14) becomes

$$\frac{d^2y}{dX^2} + f_p^+ e^{-\beta_n X} + f_p^- e^{\beta_n(X+x_p-h)} - y = 0. \quad (7.17)$$

Equation (7.17) is formally identical to Equation (7.5) in which  $-X_N$  is replaced by  $X_p - h$  and  $\beta_p$  is replaced with  $\beta_n$ . The general solution of Equation (7.17) is then

$$y = A_n \cosh X + B_n \sinh X + \frac{f_p^+ e^{-\beta_n X} + f_p^- e^{\beta_n(X+x_p-h)}}{1 - \beta_n^2}. \quad (7.18)$$

The constants  $A_n$ ,  $B_n$  can be determined by applying the two boundary conditions:

$$y = 0 \text{ at } X = 0, \quad (7.19)$$

$$\frac{dy}{dX} = -\eta_n y \text{ at } X = h - X_p, \quad (7.20)$$

where  $\eta_n = \frac{S_n L_n}{D_n}$  and  $S_n$  is the electron recombination velocity.

Considering Equation (7.19), it holds the following:

$$A_n = \frac{f_p^+ + f_p^- e^{\beta_n(X_p-h)}}{1 - \beta_n^2}. \quad (7.21)$$

Considering Equation (7.20), it holds the following:

$$\begin{aligned} A_n \sinh(h - X_p) + B_n \cosh(h - X_p) + \frac{-\beta_n f_p^+ e^{-\beta_n(h-X_p)} + \beta_n f_p^-}{1 - \beta_n^2} &= -\eta_n \\ \left[ A_n \cosh(h - X_p) + B_n \sinh(h - X_p) + \frac{f_p^+ e^{-\beta_n(h-X_p)} + f_p^-}{1 - \beta_n^2} \right]. \end{aligned} \quad (7.22)$$

Setting

$$\xi = \frac{f_p^- (\beta_n + \eta_n) - f_p^+ e^{-\beta_n(h-X_p)} (\beta_n - \eta_n)}{1 - \beta_n^2}, \quad (7.23)$$

$$\Gamma = [\sinh(h - X_p) + \eta_n \cosh(h - X_p)], \quad (7.24)$$

$$\Xi = [\cosh(h - X_p) + \eta_n \sinh(h - X_p)]. \quad (7.25)$$

The coefficient  $B_n$  is given from Equation (7.22) by the following:

$$B_n = \frac{\xi - \Gamma A_n}{\Xi}. \quad (7.26)$$

In the quasi-neutral region of the base, the current density is purely diffusive, and it can be calculated in  $X=0$ :

$$J_n(0) = q D_n \frac{1}{L_p^4} \frac{dy}{dX} \Big|_{X=0}, \quad (7.27)$$

$$J_n(0) = q D_n \frac{1}{L_n^4} \left[ B_n + \beta_n \frac{f_p^- e^{\beta_n(X_p-h)} - f_p^+}{1 - \beta_n^2} \right], \quad (7.28)$$

where  $B_n$  is given by Equation (7.26).

## 7.3 | Determination of $J_{dr}$

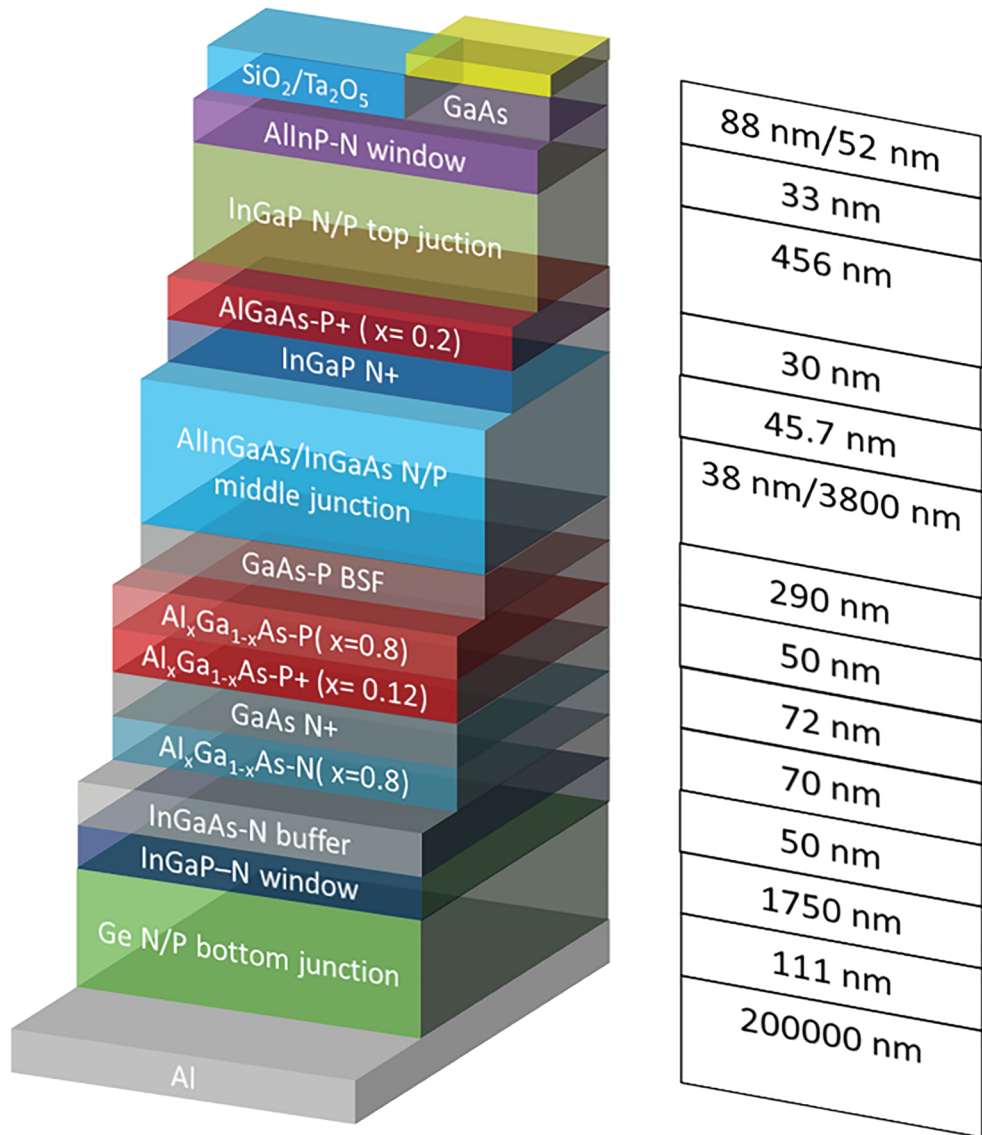
With the assumption that all the generated carries are swept in opposite directions and collected without losses (assumption 9 of Section 2), the current density generated in the depletion region is simply given by the following:

$$J_{dr}(x, \lambda) = q \left\{ \left[ F_{Nj}^+(x_N, \lambda) + F_{pj}^-(x_p, \lambda) \right] \left( 1 - e^{-2\text{Im}[k(\lambda)]w} \right) \right\}, \quad (7.29)$$

where  $w = w_n + \Delta + w_p$  (see Figure 3).

Equations (7.12) and (7.28) are simple analytical solutions of the continuity equation, which allow calculating the density

**FIGURE 4** InGaP/InGaAs/Ge TJ cell structure and related layer thicknesses. In the top cell, the BSF is constituted by a high P-doped InGaP layer, with a thickness of 12 nm. In the figure, the top cell total thickness is indicated [Colour figure can be viewed at [wileyonlinelibrary.com](http://wileyonlinelibrary.com)]



currents in each quasi-neutral region of the subcell of a MJ device, as a function of the positive and negative flows determined in each layer by SMM.

## 8 | THE TRIPLE JUNCTION INGAP/INGAAS/GE CASE STUDY

A InGaP/InGaAs/Ge triple junction solar cell, whose structure is detailed in Figure 4, is considered as a case study to demonstrate that the photon flux oscillatory terms calculated from Equations (13.14) and (13.15) are indeed negligible with respect to the photon flux in positive and negative directions calculated from Equations (13.10) to (13.13). For improving the comparison, the photon fluxes owing to the negative and to the interference between counter propagating waves have been multiplied by a factor of 10. It is also assumed to concentrate the solar light at 500x. For the homojunction InGaP top cell and for the

heterojunction AllnGaAs/InGaAs middle cell, the positive and negative photon fluxes are calculated respectively through Equations (6.7) and (6.8) and similarly the counter-propagating waves interference flux. Figure 5 clearly shows that the spectral photon flux oscillatory terms are negligible with respect to the spectral photon flux in positive and negative directions. The photon flows values are obtained by integrating the spectral photon fluxes in the wavelength range of interest. In all cases, the photon flows due to the interference between counter propagating waves are four to five orders of magnitude lower than the values of the positive flows and two to three orders of magnitude lower than the values of the negative flows (see Table 3). This case study confirms that, with good precision, it is possible to solve the continuity equation in each PV active layer of the MJ structure by using a *simplified generation function*, given by Equation (6.10), in which the positive and negative flows at the beginning and at the end of each layer can be calculated by SMM. The proposed mathematical approach allows getting simple analytical solutions of the continuity equation,

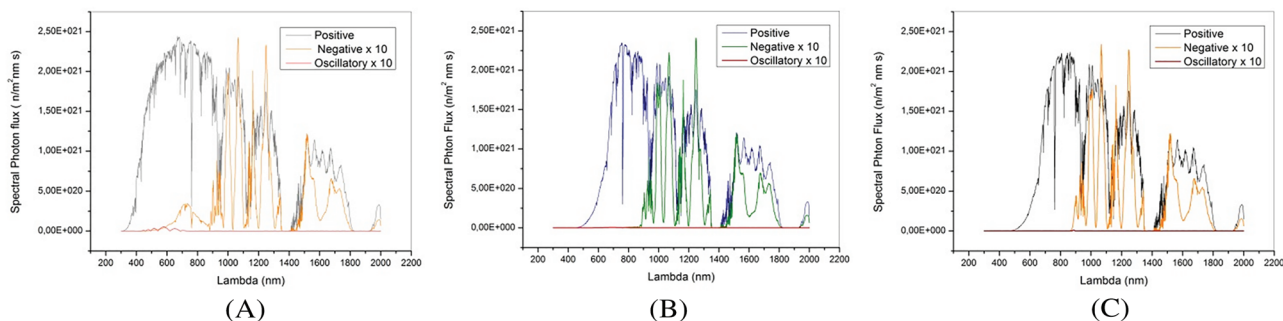


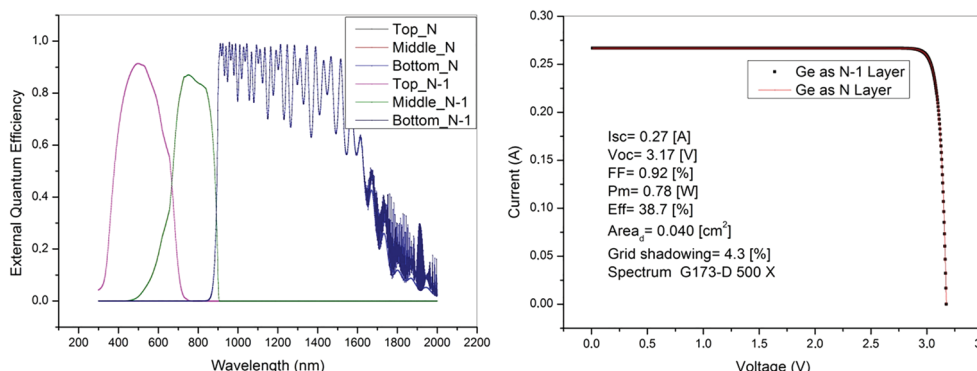
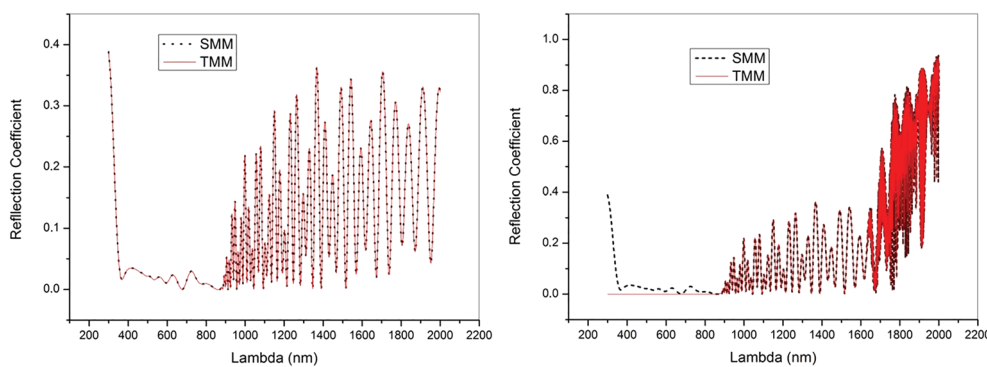
**FIGURE 5** Spectral photon fluxes at the end of the top InGaP cell (A), AlInGaAs middle emitter (B), and InGaAs middle base (C) [Colour figure can be viewed at [wileyonlinelibrary.com](http://wileyonlinelibrary.com)]

**TABLE 3** Photon flows values in InGaP, AlInGaAs and InGaAs photovoltaic active layers

Flux, ph/m <sup>2</sup> s	InGaP	AllnGaAs	InGaAs
Positive flux	$1.84 * 10^{24}$	$1.32 * 10^{24}$	$8.76 * 10^{23}$
Negative flux	$5.39 * 10^{22}$	$4.86 * 10^{22}$	$4.85 * 10^{22}$
Interference flux between counter propagating waves	$5.38 * 10^{20}$	$8.06 * 10^{19}$	$2.03 * 10^{19}$

without losing, at the same time, the accuracy for analysing the propagation of electromagnetic waves inside the solar cells structures, taking into account the interference effects.

The very low contribution of counter propagating waves in the overall photon flux is not a characteristic of specific solar cell structure: It has been also evidenced by Deparis, for a Si-based thin-film tandem solar cell.<sup>23</sup> Therefore, the proposed simplification of the generation function can be applied to any cell structure.



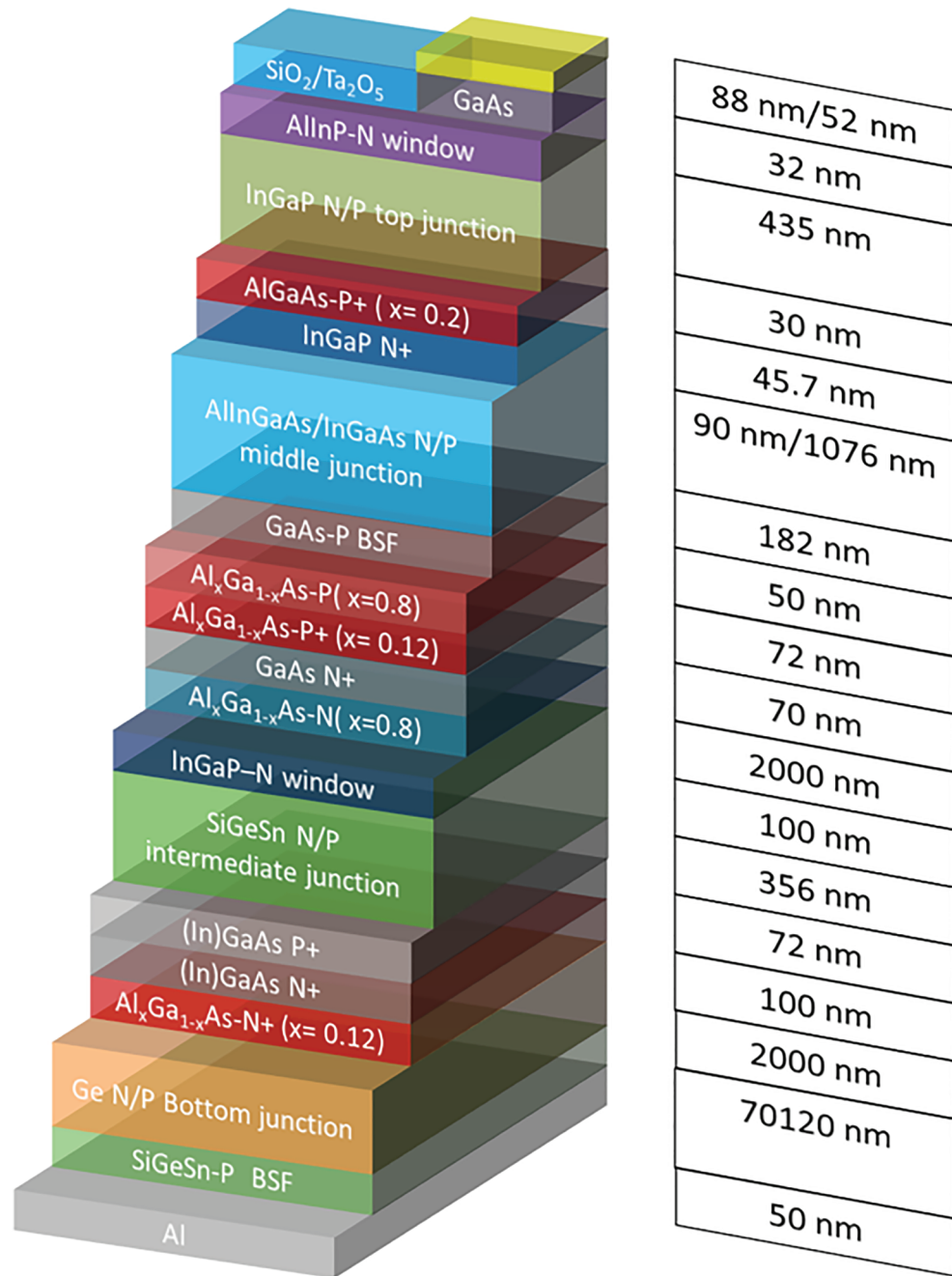
9 | ROBUSTNESS OF SMM VSTMM

In order to demonstrate the numerical stability of the SMM vs TMM, such mathematical methods have been applied to simulate the performance of a 3J InGaP/InGaAs/Ge solar cell in which the Ge substrate is first considered as the last layer (layer N) and then considered as the N-1 layer. The second case allows increasing the total thickness of the cell structure and then checking for any numerical instability. In the simulation, the current-voltage (I-V) curves have been obtained neglecting the series and shunt resistance (ideal I-V curves). Figure 6 shows that, when the Ge substrate is considered as the N-1 layer, the TMM fails in the determination of the reflectance for all the wavelength values <900 nm; on the other hand, the SMM is stable in all the wavelength range. The simulations of the TJ external quantum efficiency (EQE) and IV curve, carried out by applying SMM, give the same results regardless the Ge substrate is considered as the last layer (layer N) or as the N-1 layer (see Figure 7).

**FIGURE 6** Reflection coefficient of a 3J InGaP/InGaAs/Ge solar cell calculated by applying TMM and SMM, by considering a 200- $\mu\text{m}$ -thick Ge substrate as N layer (left) and as N-1 layer (right). To better visualize the numerical instability, the reflectance has been arbitrarily set to zero whenever the calculus started going in overflow [Colour figure can be viewed at [wileyonlinelibrary.com](http://wileyonlinelibrary.com)]

**FIGURE 7** EQE (left) and IV curve (right) of a 3J InGaP/InGaAs/Ge solar cell considering a 200- $\mu\text{m}$ -thick Ge substrate either as N layer (lines) or as N-1 layer (dots).  $T = 300\text{ K}$  [Colour figure can be viewed at [wileyonlinelibrary.com](http://wileyonlinelibrary.com)]

**FIGURE 8** Two-terminal InGaP/InGaAs/SiGeSn/Ge four junction solar cell structure and related layer thicknesses. In the top cell, the BSF is constituted by a high P-doped InGaP layer, with a thickness of 12 nm. In the SiGeSn cell, the BSF is constituted by a high P-doped SiGeSn layer, with a thickness of 20 nm. In the figure, the top cell total thickness and the SiGeSn total thickness are indicated. The substrate has been removed [Colour figure can be viewed at [wileyonlinelibrary.com](http://wileyonlinelibrary.com)]



This result corresponds to our expectations, since for a very thick substrate, the negative components of the Poynting vector are negligible. The excellent agreement among the data demonstrates the robustness of the developed mathematical code based on SMM.

## 10 | SIMULATION OF THE PERFORMANCES OF INGAP/INGAAS/SIGESN/GE SOLAR CELLS, IN 2T AND 3T CONFIGURATION

The combination of group IV and III to V elements have paved the way for developing frontier lattice matched MJ solar cells, in

particular, the InGaP/InGaAs/SiGeSn/Ge QJ ones, in which the SiGeSn plays the role of the third junction, with a 1eV energy gap ( $E_g$ ).<sup>24,25</sup> However, the realization of a 2T QJ structure, by combining IV and III to V elements in the same metal organic chemical vapour deposition (MOVPE) growth chamber is challenging, because of the cross contamination problem.<sup>26,27</sup> A 2T InGaP/InGaAs/SiGeSn/Ge solar cell structure is, for example, reported in Figure 8, in which we notice the presence of an (In)GaAs bottom TD (BTD). If the (In)GaAs layers of the BTD were kept very thin, to avoid limiting the current of the bottom Ge cell, the residual contamination present in the growth environment after the IV elements deposition could cause a polarity inversion in the (In)GaAs-P side of the BTD. In order to mitigate such a risk, an AlGaAs spacer is introduced after the group IV growth.

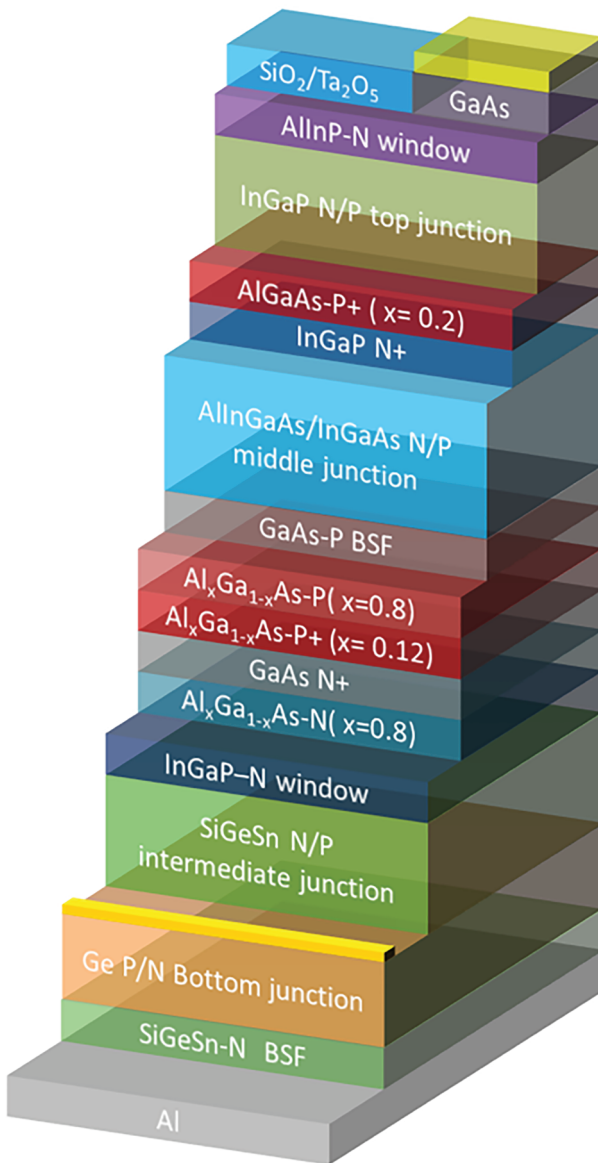


**FIGURE 9** Three-terminal InGaP/InGaAs/SiGeSn/Ge four junction solar cells structure and related layer thicknesses. In the top cell, the BSF is constituted by a high P-doped InGaP layer, with a thickness of 10 nm. In the SiGeSn cell, the BSF is constituted by a high P-doped SiGeSn layer, with a thickness of 20 nm. In the figure, the top cell total thickness and the SiGeSn total thickness are indicated. The substrate has been removed [Colour figure can be viewed at [wileyonlinelibrary.com](http://wileyonlinelibrary.com)]

88 nm/52 nm
33 nm
480 nm
30 nm
45.7 nm
90 nm/1358 nm
182 nm
50 nm
72 nm
70 nm
2000 nm
100 nm
430 nm
70530 nm
50 nm

Furthermore, the BTD must also survive the thermal MOVPE load because of the deposition of the upper layers. These questions justify the proposal of a 3T QJ, which would allow eliminating the bottom TD, and therefore, from the growth's point of view, it would present an easier and more robust QJ structure (see Figure 9). Furthermore, in this case, the current matching would be only required for the first, second, and third junctions, as the fourth junction can be independently contacted. For the 3T device, however, we have to consider the following drawbacks: (a) It presents a somewhat more complicated post-growth manufacturing process; (b) as the grid contacts are interdigitated, the grid pitch has to be larger than the case of the 2T device; and (c) the "double" grid introduces a higher shadowing. Since the performances of the QJ InGaP/InGaAs/SiGeSn/Ge solar cells in the 3T configuration have not published yet, we have applied our new mathematical approach to evaluate and compare the possible performances of the InGaP/InGaAs/SiGeSn/Ge QJ solar cell in 2T and 3T configurations. The MJ performances have been obtained by considering realistic cell parameters (see Table 4). The mobility and the lifetime have been extrapolated from the data reported in previous

studies.<sup>28-30</sup> For the Ge bottom cell, the cell parameters are different for the 2T and for the 3T QJ, as the polarity of the junctions is inverted and different doping levels are selected. For SiGeSn, experimental data on the absorption coefficient measured on MOVPE grown samples have been used, imposing a threshold absorption at 1eV.<sup>31</sup> Series resistance effect and a grid shadowing of 4% have been also included. The single diode model, no losses from shunt resistance, and good electrical performing TDs are the further simplifications assumed.

The utilized grid masks for the 2T and 3T devices are reported in Figure 10. In Table 5, the series resistance calculations are reported, according to following formula<sup>32</sup>:

$$R = \frac{R_{sh}a^2}{12} + \frac{R_m a b^2}{3t} + \frac{R_c}{S}, \quad (10.1)$$

where  $R_{sh}$  is the InGaP or Ge emitter sheet resistance (window's contribution not considered);  $R_c$  is the contact resistance;  $R_m$  is the sheet resistance of the metal  $\rho_m/w$ ,  $\rho_m$  and  $w$  are respectively resistivity

**TABLE 4** Parameters assumed in the performance evaluation of 4J-InGaP/InGaAs/SiGeSn/Ge solar cells

Cell/Parameters	$\tau_p/\tau_{rad}$ , s	$\mu_p$ , cm <sup>2</sup> /(V * s)	$S_p$ , cm/s	$\tau_n/\tau_{rad}$ , s	$\mu_n$ , cm <sup>2</sup> /(V * s)	$S_n$ , cm/s
Top-InGaP	$1 * 10^{-9}/5 * 10^{-9}$	80	$1.3 * 10^3$	$1 * 10^{-8}/1 * 10^{-7}$	1745	103
Middle-(Al)InGaAs	$8 * 10^{-10}/1.1 * 10^{-9}$	116	$10^3$	$1 * 10^{-9}/3.4 * 10^{-9}$	2950	103
Intermediate SiGeSn	$1 * 10^{-7}/1.5 * 10^{-6}$	200	$10^3$	$3 * 10^{-6}/1.5 * 10^{-5}$	1000	103
Bottom-Ge (2T)	$1 * 10^{-7}/1.5 * 10^{-6}$	209	$10^3$	$3 * 10^{-6}/1.5 * 10^{-5}$	1009	103
Bottom-Ge (3T)	$1 * 10^{-5}/1.5 * 10^{-4}$	800				

Notes. The considered life times are compared with the purely radiative lifetimes. Radiative lifetimes have been calculated by considering the following values for the *band to band* recombination coefficient:  $\beta_{Ge} = 6.4 * 10^{-14}$  cm<sup>3</sup>/s;  $\beta_{GaAs} = 7.2 * 10^{-10}$  cm<sup>3</sup>/s;  $\beta_{InGaP} = 1 * 10^{-10}$  cm<sup>3</sup>/s.

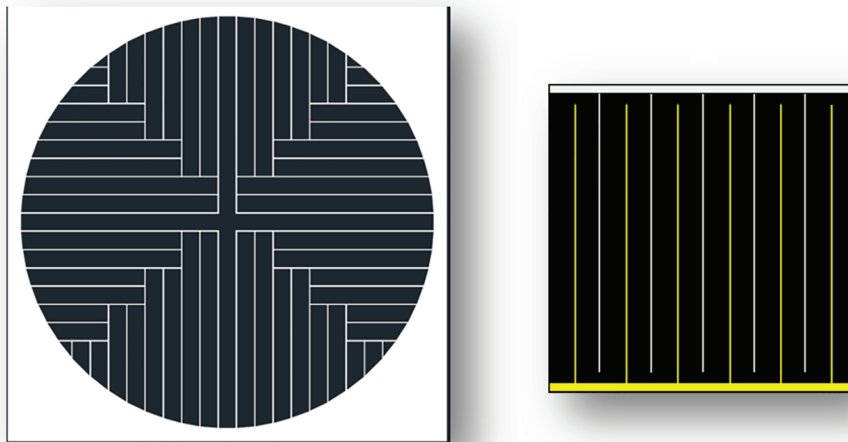


**FIGURE 10** On the left, the metallic grid utilized for the two-terminal device with a grid pitch of 100  $\mu\text{m}$ ; on the right, the metallic grid utilized for the three-terminal device, with a grid pitch of 160  $\mu\text{m}$ . Images not in scale [Colour figure can be viewed at [wileyonlinelibrary.com](http://wileyonlinelibrary.com)]

**TABLE 5** Grid main parameters and series resistance calculation according to Equation (10.1)

2-Terminal QJ		3-Terminal QJ	
Cell Dimension: 2.4 mm $\times$ 2.4 mm		Cell Dimension: 1 mm $\times$ 1 mm	
$a$ , $\mu\text{m}$	100		160 <sup>a</sup>
$b$ , $\mu\text{m}$	680		900
$t$ , $\mu\text{m}$	5		4
$R_s$ , $\Omega$	0.46		3J: 1.48 bottom J: 0.52

Notes.  $R_{sh}$  (InGaP) = 1950  $\Omega/\text{sq}$ ;  $R_{sh}$  (Ge) = 78  $\Omega/\text{sq}$ ;  $R_m$  = 0.08  $\Omega$ ;  $R_c$  =  $5 * 10^{-6}$   $\Omega \text{ cm}^2$ .

<sup>a</sup>For the calculus of the grid shadowing,  $a = 80 \mu\text{m}$ .

and thickness of the metal;  $a$  is the grid pitch;  $t$  is the grid width;  $b$  is the average grid length;  $S = t/a$  is the grid shadowing factor.

For the 3T device, the series resistance contribution has been calculated for the three junctions connected in series (top, middle, and intermediate) and for the Ge bottom junction. Note that in order to mitigate the series resistance problem of the 3T device, the cell area has been reduced to 1 mm<sup>2</sup> with respect to the value of 5.76 mm<sup>2</sup> related to the 2T device. Figure 11 shows the EQE of the 2T and of the 3T InGaP/InGaAs/SiGeSn/Ge QJ cell, while in Figure 12, the related I-V curves are depicted. It is worthwhile to point out that the efficiency values have been calculated by assuming a conventional SiO<sub>2</sub>/Ta<sub>2</sub>O<sub>5</sub> antireflective coating, which shows a nonideal reflectivity curve in the wavelength range 900 to 1600 nm. As expected, the best efficiency value calculated for the 3T QJ is slightly lower than the

value obtained for the 2T QJ (44.9% vs 45.1%) because of the series resistance losses. Nevertheless, in spite of the higher series resistance, the almost similar performances of the 2T and 3T devices indicate that the 3T QJ can be an alternative solution to the 2T QJ cell, even for high concentration operating conditions, in case it will be difficult to realize an "efficient" TD between the third and four junction in the 2T QJ solar cell.

The performance obtained on the 2T InGaP/InGaAs/SiGeSn/Ge QJ has also been compared with those published by Wilson et al.,<sup>33</sup> under AM1.5D illumination at 1000 sun concentration and considering a 4% grid shadowing. The one-sun current density and efficiency values calculated in<sup>33</sup> were respectively 13.9 mA/cm<sup>2</sup> and 48.6% versus 12.5 mA/cm<sup>2</sup> and 45.1 % calculated in this contribution. The lower current value calculated in our simulation, and therefore, the

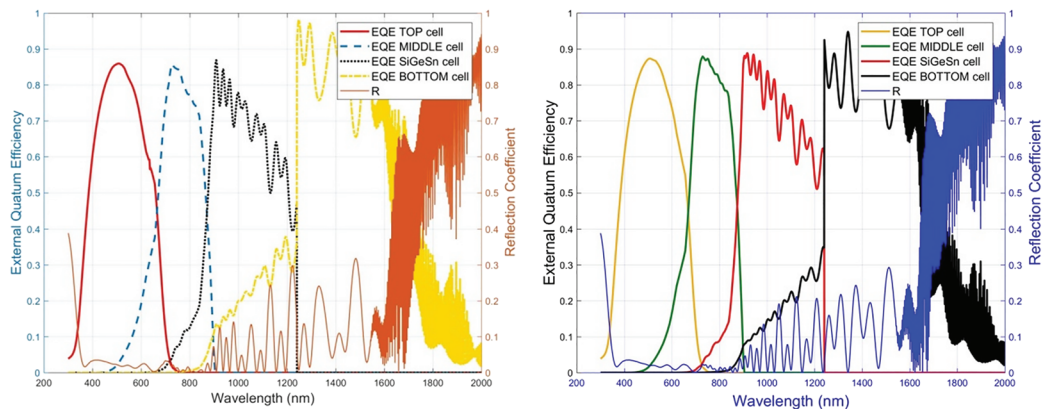


**FIGURE 11** Simulated EQE and reflection coefficient of a InGaP/InGaAs/SiGeSn/Ge four junction solar cell in a 2T (left) and 3T (right) configurations [Colour figure can be viewed at [wileyonlinelibrary.com](http://wileyonlinelibrary.com)]

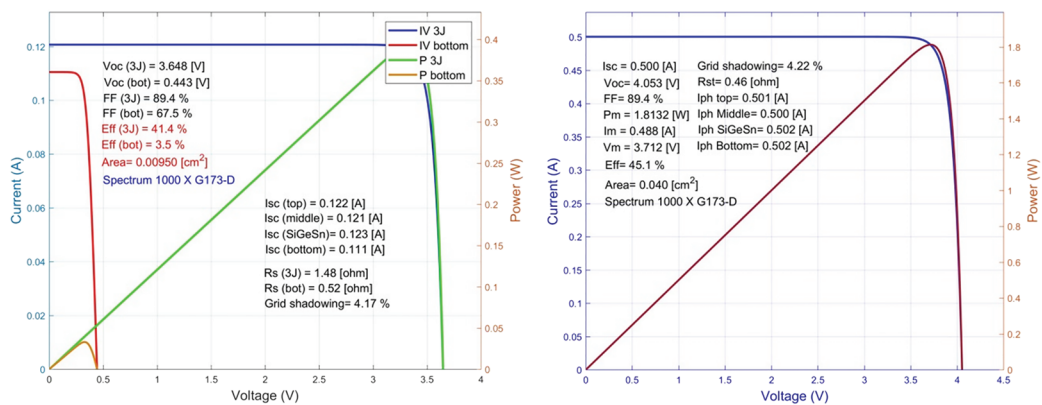


**FIGURE 12** IV curves of the InGaP/InGaAs/SiGeSn/Ge solar cell in 3T (left) and 2T (right) configurations.  $T = 300$  K [Colour figure can be viewed at [wileyonlinelibrary.com](http://wileyonlinelibrary.com)]

lower efficiency value can be mainly attributed to the utilization of a  $\text{SiO}_2/\text{Ta}_2\text{O}_5$  coating instead of the  $\text{MgF}_2/\text{ZnS}$  one, as utilized in Wilson et al.<sup>33</sup> Since the  $\text{SiO}_2/\text{Ta}_2\text{O}_5$  planar coating did not show optimized reflectance values in the wavelength range where the SiGeSn and Ge sub cells are active, this condition forced to limit the thickness of the InGaP and InGaAs junctions and then the overall current. It is straightforward to check that by assuming the same  $\text{MgF}_2/\text{ZnS}$  coating, in order to reach the same current density measured by Wilson et al<sup>33</sup> and preserving the high fill factor value obtained in our simulation (by considering an InGaAs limited QJ cell), our calculation would show an efficiency value potentially over 50%, in agreement with the simulation reported by Kurtz et al<sup>34</sup> and by Geisz and Friedman<sup>35</sup> on QJ cells with a 1-eV  $E_g$  third junction. Overcoming the 50% efficiency threshold is of course a major goal for present-day research on MJ solar cells.

## 11 | CONCLUSION

For developing next generation MJ solar cells, it is very useful to provide robust mathematical methods, which adopt simplified but sufficiently precise analytical solutions. Owing to its simplicity, the

analytical Hovel model has been widely and successfully applied; however, it is not suitable in the performance simulation of QJ solar cells where the interference effects can be important. The most used TMM can present numerical instability when applied to MJ solar cells. Furthermore, the electromagnetic radiations calculated by this method, when inserted in the semiconductor continuity equations to determine the photocarrier generation gives rise to complicated solutions even for relatively few layers. In this work, a simplified SMM has been successfully implemented to overcome the TMM numerical instability, which arises when the MJ solar cell reaches a certain thickness. In order to demonstrate the robustness of the method, the SMM has been applied to TJ solar cell structures in which even a hundred micron thick layer has been included. We have also demonstrated that the *generation function* calculated by applying SMM can be notably simplified, once the interference of counter propagating waves in the active layers of the solar cell can be omitted, and it is possible to get sufficiently precise analytical solutions of the continuity equation in the quasi-neutral regions of the subcells of the MJ device. The new mathematical approach has then been applied to simulate the performance of QJ InGaP/InGaAs/SiGeSn/Ge solar cells both in two and 3T configuration. Efficiency values as high as 50% can be obtained on the 2T device, with proper antireflective coating. A slightly lower

efficiency value has been evaluated on a 3T QJ solar cell, owing to the higher series resistance. However, the almost similar performances of the 2T and 3T devices indicate that the 3T QJ is an alternative solution to the 2T QJ, in case it will be difficult to realize an "efficient" TD between the third and four junctions. The presented new mathematical approach can be easily implemented in commercial software platforms and therefore successfully applied to optimize the structure of next generation MJ solar cells, with a very good trade-off between computing time and accuracy.

## ACKNOWLEDGEMENT

This work has been financed by the Research Fund for the Italian Electrical System in compliance with the Decree of Minister of Economic Development April 16, 2018.

## ORCID

Gianluca Timò  <https://orcid.org/0000-0001-9237-7961>

## REFERENCES

- Li ZQ, Xiao YG, Lestrade M, Li ZMS, "2D-simulation of inverted metamorphic GaInP/GaAs/GaInAs triple junction solar cell," in *Conference Record of the IEEE Photovoltaic Specialists Conference*, 2008.
- Bozzola A, Liscidini M, Andreani LC. Broadband light trapping with disordered photonic structures in thin-film silicon solar cells. *Prog Photovoltaics Res Appl.* 2014;22(12):1237-1244.
- Hovel HJ. *Semiconductors and semimetals: solar cells*. London: Academic Press Inc; 1975.
- Harbecke B. Coherent and incoherent reflection and transmission of multilayer structures. *Appl Phys B.* 1986;39:165-170.
- Knittl Z. *Optics of thin films*. 1976.
- Ohta K, Ishida H. Matrix formalism for calculation of electric field intensity of light in stratified multilayered films. *Appl Optics.* 1990;29(13):1952-1959.
- Letay G, Breselge M, Bett AW. Calculating the generation function of III-V solar cells. *3rd World Conf Photovoltaic Energy Conversion, 2003 Proc.* 2003;1:741-744.
- Centurioni E. Generalized matrix method for calculation of internal light energy flux in mixed coherent and incoherent multilayers. *Appl Optics.* 2005;44(35):7532-7539.
- Bhattacharya I, "Florida State University libraries design and modeling of very high- efficiency multijunction solar cells," 2013.
- Garcia I, Geisz J, Steiner M, Olson J, Friedman D, Kurtz S, "Design of semiconductor-based back reflectors for high Voc monolithic multijunction solar cells BT - 38th IEEE Photovoltaic Specialists Conference, PVSC 2012, June 3, 2012 - June 8, 2012," no. June, pp. 2042-2047, 2012.
- Pettersson LAA, Roman LS, Inganäs O. Modeling photocurrent action spectra of photovoltaic devices based on organic thin films. *J Appl Phys.* 1999;86(1):487-496.
- Brendel R, Hirsch M, Plieninger R, Werner JH. Quantum efficiency analysis of thin-layer silicon solar cells. *IEEE Trans Electron Devices.* 1996;43(7):1104-1113.
- Lumb MP, Bailey CG, Adams JG, et al. Extending the 1-d hovel model for coherent and incoherent back reflections in homojunction solar cells. *IEEE J Quantum Electron.* 2013;49(5):462-470.
- Bozzola A, Kowalczewski P, Andreani LC. Towards high efficiency thin-film crystalline silicon solar cells: the roles of light trapping and non-radiative recombinations. *J Appl Phys.* 2014;115(9):094501-1-094501-10.
- Timò G, Andreani L, "Simulation of the performances of multi-junction solar cells with improved voltage by transfer and scattering matrix methods," *Proc. IEEE 44th Photovolt. Spec. Conf.*, 1, 1, 2017.
- Yuffa AJ, Scales JA. Object-oriented electrodynamic S-matrix code with modern applications. *J Comput Phys.* 2012;231(14):4823-4835.
- Shigyo N, Tanimoto H, Norishima M, Yasuda S. Minority carrier mobility model for device simulation. *Solid State Electron.* 1990;33(6):727-731.
- Léty G, Hermle M, Bett AW. Simulating single-junction GaAs solar cells including photon recycling. *Prog Photovoltaics Res Appl.* 2006;14(8):683-696.
- Steiner MA, Geisz JF, García I, Friedman DJ, Duda A, Kurtz SR. Optical enhancement of the open-circuit voltage in high quality GaAs solar cells. *J Appl Phys.* 2013;113(12):123109-1-123109-11.
- Friedman DJ, Geisz JF, Steiner MA. Effect of luminescent coupling on the optimal design of multijunction solar cells. *IEEE J Photovoltaics.* 2014;4(3):986-990.
- Nelson J. Over the limit: strategies for high efficiency. In: *The Physics of Solar Cells*. London: Imperial College Press; 2012:289-325.
- Kowalczewski P, Redorici L, Bozzola A, Andreani LC. Silicon solar cells reaching the efficiency limits: from simple to complex modelling. *J Opt (United Kingdom).* 2016;18(5):054001-1-054001-11.
- Deparis O. Poynting vector in transfer-matrix formalism for the calculation of light absorption profile in stratified isotropic optical media. *Opt Lett.* 2011;36(20):3960-3962.
- Fang Y-Y, Xie J, Tolle J, et al. "Molecular-based synthetic approach to new group IV materials for molecular-based synthetic approach to new group IV materials for high-efficiency, lowcost solar cells and Si-based optoelectronics". 2008: 16095-16102.
- Philips SP, Baudrit M, Hillerich K, et al. "CPVMatch-concentrating photovoltaic modules using advanced technologies and cells for highest efficiencies," *32nd Eur. Photovolt. Sol. Energy Conf. Exhib. (EU PVSEC 2016)*, vol.200040200, 2016: 1393-1398.
- Welser E, Guter W, Wekkeli A, Dimroth F. Memory effect of Ge in III-V semiconductors. *J Cryst Growth.* 2008;310(23):4799-4802.
- Timò G, Abagnale G, Armani N, Calicchio M, Schineller B, "MOVPE SiGeSn development for the next generation four junction solar cells," *AIP Conf. Proc.*, 2012, 2018.
- Levinshtein M, Rumyantsev S, Shur M. *Handbook Series on Semiconductor Parameters*. 2 Singapore: World Scientific; 1996.
- Elfify D, Yamaguchi M, Sasaki T, et al. Theoretical optimization of base doping concentration for radiation resistance of InGaP subcells of InGaP/GaAs/Ge based on minority-carrier lifetime. *Jpn J Appl Phys.* 2010;49(12):121201-1-121201-7.
- Yoon H Edmondson KM, Kinsey GS, King RR, Hebert P, Ahrenkiel RK, Cavigchi BT, Karam NH, "Minority carrier lifetime and radiation damage coefficients of germanium," 2005: 842-845.
- Timò G, Abagnale G, Calicchio M, "to be published."
- Liu W, Li Y, Chen J, Chen Y, Wang X, Yang F. Optimization of grid design for solar cells. *J Semicond.* 2010;31(1):3-6.
- Wilson T, Thomas T, Führer M, Ekins-Daukes NJ, Roucka R, Clark A, Johnson A, Hoffman R, Begarney D, "Single and multi-junction solar cells utilizing a 1.0 eV SiGeSn junction," in *AIP Conference Proceedings*, 2016, vol. 1766.
- Kurtz SR, Myers D, Olson JM, "Projected performance of three- and four-junction devices using GaAs and GaInP," in *Conference Record of the IEEE Photovoltaic Specialists Conference*, 1997: 875-878.
- Geisz JF, Friedman DJ. III-N-V semiconductors for solar photovoltaic applications. *Semicond Sci Technol.* 2002;17(8):769-777.

**How to cite this article:** Timò G, Martinelli A, Andreani LC. A new theoretical approach for the performance simulation of multijunction solar cells. *Prog Photovolt Res Appl*. 2020;28: 279–294. <https://doi.org/10.1002/pip.3225>

all the ratios  $\frac{N_{N-1}^+}{N_N^+}$ ,  $\frac{N_{N-2}^+}{N_N^+}$ , ...,  $\frac{N_1^+}{N_N^+}$  and  $\frac{N_{N-1}^-}{N_N^-}$ ,  $\frac{N_{N-2}^-}{N_N^-}$ , ...,  $\frac{N_1^-}{N_N^-}$ , that is, the electric field at the end of each solar cell layer. The same procedure can be applied to calculate the electric field for TM and TE mode, by using the proper relationship reported in Table 1, at the beginning of each solar cell layer.

## APPENDIX A

Let us consider to calculate the radiation at the end of each layer. The solution of the linear equation system given Equation (13.3) is easily obtained pointing out that

$$\begin{bmatrix} N_0^+ \\ N_0^- \end{bmatrix} = M_1 \begin{bmatrix} N_1^+ \\ N_1^- \end{bmatrix}, \quad \begin{bmatrix} N_1^+ \\ N_1^- \end{bmatrix} = M_2 \begin{bmatrix} N_2^+ \\ N_2^- \end{bmatrix} \rightarrow \begin{bmatrix} N_0^+ \\ N_0^- \end{bmatrix} = M_1 M_2 \begin{bmatrix} N_2^+ \\ N_2^- \end{bmatrix} \quad (13.16)$$

Therefore,

$$\begin{bmatrix} N_0^+ \\ N_0^- \end{bmatrix} = M_1 M_2 .. M_N \begin{bmatrix} N_N^+ \\ N_N^- \end{bmatrix}, \quad (13.17)$$

$$\begin{bmatrix} N_0^+ \\ N_N^- \\ N_0^- \\ N_N^+ \end{bmatrix} = M \begin{bmatrix} 1 \\ 0 \end{bmatrix}, \quad (13.18)$$

where

$$M = M_1 M_2 .. M_N \rightarrow M = \begin{bmatrix} M_{11} & M_{12} \\ M_{21} & M_{22} \end{bmatrix} \quad (13.19)$$

From Equations (13.18) and (4.1), it follows

$$\frac{N_0^+}{N_N^+} = M_{11}, \rightarrow N_N^+ = \frac{N_0^+}{M_{11}}, \quad \frac{N_0^-}{N_N^-} = M_{21} \rightarrow N_0^- = N_N^+ M_{21}. \quad (13.20)$$

The term  $N_0^+$  can be calculated through the solar radiation Poynting vector; therefore, from Equation (13.20), we can determine  $N_N^+$  and  $N_0^-$ .

Hence, we can calculate with the following procedure:

$$\begin{bmatrix} N_{N-1}^+ \\ N_N^+ \\ N_{N-1}^- \\ N_N^- \end{bmatrix} = M_N \begin{bmatrix} 1 \\ 0 \end{bmatrix}, \rightarrow \begin{bmatrix} N_{N-2}^+ \\ N_N^+ \\ N_{N-2}^- \\ N_N^- \end{bmatrix} = M_{N-1} \begin{bmatrix} N_{N-1}^+ \\ N_N^+ \\ N_{N-1}^- \\ N_N^- \end{bmatrix} \rightarrow \begin{bmatrix} N_1^+ \\ N_N^+ \\ N_1^- \\ N_N^- \end{bmatrix} = M_2 \begin{bmatrix} N_2^+ \\ N_N^+ \\ N_2^- \\ N_N^- \end{bmatrix} \quad (13.21)$$

## APPENDIX B

S-matrix elements considering the complex amplitudes of the forward and backward waves at the beginning of the layers:

$$S_j(1,1) = \frac{(w_j - w_{j-1})(\psi_{j-1}^+)^2 + (w_j + w_{j-1})S_{j-1}(1,1)}{(w_j + w_{j-1})(\psi_{j-1}^+)^2 + (w_j - w_{j-1})S_{j-1}(1,1)}. \quad (13.22)$$

Getting  $S_{j-1}(1,1)$  from  $S_j(1,1)$ ,

$$S_{j-1}(1,1) = \frac{(\psi_{j-1}^+)^2 [(w_j + w_{j-1}) S_j(1,1) - (w_j - w_{j-1})]}{[(w_j + w_{j-1}) - S_j(1,1)(w_j - w_{j-1})]}. \quad (13.23)$$

For  $J = N$ , recalling that  $S_N(1,1) = 0$ , it follows:

$$S_{N-1}(1,1) = \frac{(w_{N-1} - w_N)}{(w_{N-1} + w_N)} (\psi_{N-1}^+)^2, \quad (13.24)$$

$$S_j(2,1) = \frac{2w_j \psi_{j-1}^+ S_{j-1}(2,1)}{(w_j - w_{j-1}) S_{j-1}(1,1) + (w_j + w_{j-1})(\psi_{j-1}^+)^2} \quad (13.25)$$

Getting  $S_{j-1}(2,1)$  from  $S_j(2,1)$ ,

$$S_{j-1}(2,1) = \frac{S_j(2,1) [(w_j - w_{j-1}) S_{j-1}(1,1) + (w_j + w_{j-1})(\psi_{j-1}^+)^2]}{2w_j \psi_{j-1}^+}. \quad (13.26)$$

For  $J = N$ , recalling that  $S_N(2,1) = 1$  and by considering Equation (13.25), it follows:

$$S_{N-1}(2,1) = \frac{2w_{N-1}}{w_N + w_{N-1}} \psi_{N-1}^+. \quad (13.27)$$